Electrochemistry Communications 179 (2025) 108023

Contents lists available at ScienceDirect

Electrochemistry Communications

journal homepage: www.elsevier.com/locate/elecom

Reversible molten carbonate cells: Testing and preliminary formulation of a kinetic model

Lucia Cardona [a], Fiammetta Rita Bianchi [a,*], Emilio Audasso [b], Dario Bove [a], Sung Pil Yoon [b], Barbara Bosio [a]

[a] Department of Civil, Chemical and Environmental Engineering (DICCA), University of Genoa, Via Opera Pia 15, Genoa 16145, Italy
[b] Hydrogen-Fuel Cell Research Center, Korea Institute of Science and Technology, 5 Hwarangno 14-gil, Seongbukgu, Seoul, Republic of Korea

ARTICLE INFO

Keywords:
Reversible molten carbonate cell
IV curve model
Kinetic reaction path
Electrochemical characterization
Butler-Volmer equation

ABSTRACT

Reversible molten carbonate cell technology allows for dual operation depending on the applied polarization, alternating between Gas to Power mode as a fuel cell and Power to Gas mode as an electrolysis cell. While the first has already been used in industrial applications, the second is emerging as a promising solution for energy storage and direct syngas production from a CO_2-rich process waste stream despite several issues in effective operation. This work aims at the characterization of the reversible system operation, coupling experimental observations with a theoretical phenomenological analysis. A cell composed of state-of-the-art materials is tested, recording the electrochemical performance under variable working conditions. A rigorous discussion on the oxygen and fuel electrode reaction paths results in a preliminary kinetic formulation derived from the Butler-Volmer equation. The model considers innovatively specific equations and kinetic parameters for the anodic and the cathodic polarization of each electrode, which permits predicting the asymmetric behaviour of the cell when switching between fuel cell and electrolysis mode. Since alternating the operation mainly involves a change in the fuel electrode feed, a sensitivity analysis is performed at variable hydrogen and CO_2 compositions. Increasing hydrogen content favours the reaction evolution by avoiding starvation in fuel cell mode, while it shows an indirect influence in electrolysis by improving the diffusion of reactants. The CO_2 effect is more emphasised during electrolysis mode, resulting in the limiting reactant under the considered conditions, while it has an almost negligible dependence in a fuel cell.

1. Introduction

Molten carbonate cells are electrochemical devices commonly working at 600–650 °C that can operate in reversible mode. In fuel cell mode (i.e., the direct operation), the chemical energy of the inlet reactants is converted into electrical energy while simultaneously allowing for CO_2 capture. In electrolysis mode (i.e., the reverse operation), the cell produces syngas or, after purification steps, pure H_2 when an external energy source is provided. As schematized in Fig. 1 for both modi operandi, the cell consists of a Fuel Electrode (FE) and an Oxygen Electrode (OE) usually composed of Ni and NiO, respectively, referring to the state-of-the-art materials. They are separated by a ceramic matrix that hosts the molten carbonate electrolyte [1].

Several development projects are being and have been carried out on Molten Carbonate Fuel Cells (MCFCs) due to their potential to generate energy while capturing CO_2 from exhaust gases [2–7]. Indeed, this technology is already well-established as a power generator, with multiple MCFC plants currently in operation [8–12]. Additionally, they have been tested for naval propulsion, with the first vessel to utilize MCFC technology being the Viking Lady, which has been recognized as the first environmentally friendly ship of its kind [13]. Currently, however, the main goal of MCFC use is to extend their application to Carbon Capture and Storage (CCS) to promote CO_2 reuse and close the carbon loop [14–17]. Several possible fields for CCS through MCFC technology have been investigated, including but not limited to the steel industry [18], natural gas power plants [19], cement manufacturing [20,21], coal-based power generation [22], maritime sector [23–26], power and hydrogen generation [27]. On the contrary, both electrolysis mode and use as reverse cells are still under study. Their application should enable highly efficient hydrogen and syngas production since the electricity demand decreases by exploiting the available heat at high working temperatures. For instance, Molten Carbonate Electrolysis Cell (MCEC) technology results in a promising off-gas recovery system for H_2/CO

* Corresponding author.
E-mail address: fiammettarita.bianchi@unige.it (F.R. Bianchi).

https://doi.org/10.1016/j.elecom.2025.108023
Received 13 May 2025; Received in revised form 31 July 2025; Accepted 4 August 2025
Available online 6 August 2025

Nomenclature

A	Arrhenius constant [variable according to reaction]
C_{sur}	Surface concentration [mol m^{-3}]
C_{bulk}	Bulk concentration [mol m^{-3}]
$\mathscr{D}_{mix}$	Diffusion coefficient in a mixture [m^2 s^{-1}]
$\mathscr{D}$	Molecular diffusion coefficient [m^2 s^{-1}]
d	Electrode thickness [m]
E_{act}	Activation energy [J mol^{-1}]
ΔE	Equilibrium cell voltage [V]
ΔE^0	Reversible cell potential [V]
F	Faraday constant [C mol^{-1}]
ΔG^{WGS}	WGS Gibbs energy variation [J mol^{-1}]
K	Material transport coefficient [m s^{-1}]
K_{eq}^{WGS}	WGS equilibrium constant [−]
J	Current density [A m^{-2}]
J_0	Exchange current density [A m^{-2}]
J_{LIM}	Limiting current density [A m^{-2}]
M	Molecular weight [g mol^{-1}]
N	Molar flow rate [mol s^{-1}]
P	Pressure [atm]
R	Ideal gas constant [J $(mol\ K)^{-1}$]
R_Ω	Specific ohmic resistance [Ω m^2]
S	Active area [m^2]
T	Temperature [K]
V	Cell voltage [V]
v_r	Reaction rate [mol (s^{-1} m^{-2})]
w	Atomic diffusion volume [−]
X	Reaction extent [mol s^{-1}]
y	Molar fraction [−]
z	Charge number [−]

Greek letters

α	Reaction order [−]
β	Charge transfer coefficient [−]
γ	Kinetic constant [variable according to reaction]
ε	Electrode porosity [−]
η	Electrode overpotential in Butler-Volmer eq. [V]
η_a	Activation overpotential [V]
η_c	Diffusion overpotential [V]
η_Ω	Ohmic overpotential [V]
ν	Stochiometric coefficient [−]
τ	Electrode tortuosity [−]

syngas production from industrial waste streams [28]. Power to Methane application based on molten carbonate electrolysers was successfully validated, optimizing the internal heat management and maximizing the process efficiency [29]. Moreover, powering through renewables makes the system environmentally sustainable [30]. Further benefits consist of the absence of noble metals as catalysts and the possibility of adapting the existing MCFC plants in reverse mode for large-scale hydrogen production [31–33].

Molten carbonate cell technology has demonstrated a wide applicability in different fields. However, it is crucial to conduct further in-depth analysis. Molten carbonate fuel cell performance has been analysed in several research works [34–37], while electrolysis operation has been less investigated from both an experimental and a theoretical point of view. Cell reversible behaviour has been studied by testing the effects of working conditions on power and specific energy consumption [38–40] and modelling the performance [41,42]. Moreover, feasibility analysis has also been performed for specific application fields [43,44]. Nevertheless, these studies have usually assumed a simplified electrochemical model with constant polarization losses. To the best of the authors' knowledge, multi-dimensional numerical studies on MCEC performance [45,46] and specific algorithms for MCEC system control are also quite rare, different from other cell technologies [47–50]. Electrochemical kinetic models validated on MCFC operation have been usually used in a reversible application. Nevertheless, as demonstrated in [51,52], applying such models to the electrolysis operation implies significant errors in the prediction, which confirms the need for specific formulations of each cell operation.

With the aim of overcoming this knowledge gap, the research paper presents a preliminary kinetic formulation for reversible molten carbonate cells that can model the asymmetric operation experimentally observed in the literature when switching from fuel cell to electrolysis mode. A theoretical formulation derived from the electrochemistry principles was initially discussed for forecasting the cell overpotentials. Referring to possible reaction paths at the fuel and oxygen electrode reported in previous references, a preliminary model validation was performed on a lab-scale cell tested at common working conditions. To underline the possible applications of the developed tool, the effects of fed syngas composition were theoretically evaluated and correlated to the measured cell voltage. The presented model might consist of the basis for the next studies involving a multidimensional approach to locally predict the main physicochemical parameters and detect the specific kinetic reaction paths dependent on the materials used.

2. Experimental test plan

All experimental tests were performed at the Korea Institute of

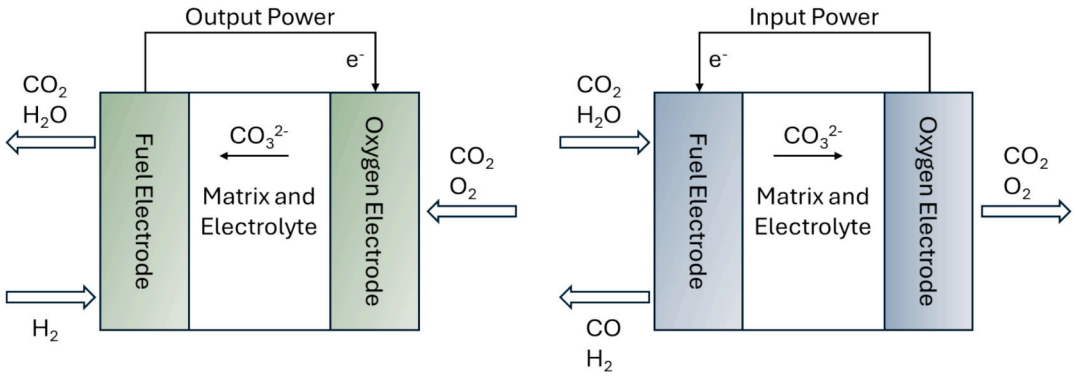

Fig. 1. Reversible molten carbonate cell operation resulting in fuel cell on the left side and electrolysis cell on the right side.

Science and Technology (KIST) in Seoul (South Korea). The single cell, with an active area of 100 cm^2, was assembled using the materials provided by KSEP (South Korea), as listed in Table 1. The cell assembly followed a meticulous process that included a preliminary investigation of cell green components: (i) determining the size, (ii) measuring the thickness of the components and current collectors, (iii) comparing these measurements to the depth of the frame that housed the cell, and (iv) evaluating the porosity. The cell was then assembled in a sandwich-like structure (Fig. 2.***A***). In particular, the anode side was placed at the bottom, ensuring that the combined thickness of the electrode and each current collector matched the depth of the frame. The matrix, electrolyte, and oxygen electrode were sequentially placed on top. The amount of electrolyte ($(Li_{0.62}K_{0.38})CO_3$) was weighted based on the area, porosity, and thickness measurements to impregnate, in terms of void volume, fully the matrix (100 %), 20 % of the oxygen electrode and 10 % of the fuel electrode.

The cell was then placed within the cell frame and maintained at a sealed pressure of 0.2 MPa using an air cylinder. Following a controlled and slow temperature ramp to remove organics inside the various components and melt the carbonates (cell electrolyte), the temperature was set to 650 °C. The inlet gases for both the fuel and oxygen compartments were supplied at controlled flow rates. For the fuel electrode flow, the inlet gas compositions were set under dry conditions; downstream of the flow meters, a humidifier allowed the water compositions to be set by adjusting the temperature and reaching the saturation point. The cell was connected to a potentiostat (*ELS300Z ELTO DC Electronics Co.*as), a frequency response analyser (*FRA 1255B Solartron Co*) and a gas chromatograph (*789 A Agilent Tech.*), as shown in Fig. 2.***B***. The voltmeter was used to impose an external current and measure the cell voltage, allowing for the analysis of cell performance. The frequency response analyser enabled frequency variation from 10 kHz to 0.01 Hz at the Open Circuit Voltage (OCV), recording Electrochemical Impedance Spectroscopy (EIS) spectra.

The experimental campaign focused on evaluating the cell performance in both operating modes (i.e., fuel cell and electrolysis). As previously mentioned, the operating conditions were set at 650 °C and 1 atm. Focusing on the influence of FE inlet gases on cell performance (Table 2), the reference conditions were systematically changed in terms of gas composition (balancing with nitrogen) and flow rate.

However, after the cell startup and before starting the effective characterization of the electrochemical kinetics, a preliminary evaluation of the system operation was performed at reference compositions. Internal and polarization resistances were evaluated at OCV through EIS measurements; gas chromatography analysis was carried out to assess N_2 crossover at the fuel electrode.

3. Kinetic theoretical formulation

Analysing the electrochemical reactions in the fuel cell mode (direct direction in ***Eq. 1***-***Eq. 2***-***Eq. 3***), the hydrogen is oxidized at the fuel electrode by producing water and the carbon dioxide is separated from the oxygen electrode to the fuel electrode. The electrolysis operation is based on the water splitting to produce molecular hydrogen and oxygen as well as to transfer the carbon dioxide from the fuel electrode to the oxygen electrode (inverse direction in ***Eq. 1***-***Eq. 2***-***Eq. 3***).

$$\text{Global cell } H_2 + \frac{1}{2}O_2 + CO_2 \underset{\text{MCFC}}{\overset{\text{MCEC}}{\leftrightarrows}} H_2O + CO_2 \tag{1}$$

$$\text{Oxygen electrode } CO_2 + 2e^- + \frac{1}{2}O_2 \underset{\text{MCFC}}{\overset{\text{MCEC}}{\leftrightarrows}} CO_3^{2-} \tag{2}$$

$$\text{Fuel electrode } H_2 + CO_3^{2-} \underset{\text{MCFC}}{\overset{\text{MCEC}}{\leftrightarrows}} H_2O + CO_2 + 2e^- \tag{3}$$

Moreover, the reaction environment at the fuel electrode allows the Water Gas Shift (WGS) to develop in both operations as well (***Eq. 4***). It is noteworthy that the CO/CO_2 electrochemical reaction can be considered negligible at the Ni fuel electrode, resulting in a much slower rate than hydrogen evolution at low current densities [45].

$$\text{Fuel electrode } H_2O + CO \leftrightarrow H_2 + CO_2 \tag{4}$$

In general terms, the cell voltage V is the algebraic sum of the equilibrium value and a series of penalizing overpotentials that are summed in the case of electrolysis mode and subtracted in the case of fuel cell mode (***Eq. 5***).

$$\begin{aligned} V &= \Delta E \pm \sum \left(\eta_\Omega + \eta_a + \eta_c\right) \\ &= \Delta E \pm \sum \left(\eta_\Omega + \eta_{a(FE)} + \eta_{c(FE)} + \eta_{a(OE)} + \eta_{c(OE)}\right) \end{aligned} \tag{5}$$

Where the equilibrium voltage ΔE derives from the Nernst equation, while the overpotentials η are computed by the Ohm law and the Butler-Volmer equation: the first is representative of charge migration resistances of the overall cell by η_Ω, the second considers gas transport and reaction resistances in terms of η_c and η_a, respectively, for each electrode (FE – Fuel electrode, OE – Oxygen Electrode). Note that the current density absolute value is sometimes used in the following formulations to always have a positive value, without considering the current sign imposed by the Butler-Volmer equation for the direct and the indirect reaction, as defined below, or the sign convention used in polarization curve experimental profiles.

The equilibrium conditions are described by Nernst equation for both operations (***Eq. 6***) [53].

$$\Delta E = \Delta E^0 + \frac{RT}{zF}\ln\left(\frac{P_{H_2}P_{CO_2(OE)}P_{O_2}^{0.5}}{P_{H_2}P_{CO_2(FE)}}\right) \tag{6}$$

Where ΔE^0 is the reversible potential, computed as a function of temperature T, R the ideal gas constant, z the charge number, F the Faraday constant and P the partial pressure of i-th component.

To evaluate the cell electrochemical performance, it is required to consider different losses, namely ohmic, activation and diffusion overpotentials. The first one is related to the voltage drop due to the transport of the charged species within the cell; it is represented by the following equation (***Eq. 7***).

$$\eta_\Omega = R_\Omega |J| \tag{7}$$

Where R_Ω is the specific ohmic resistance of the whole cell, usually variable with temperature, and J the current density.

Table 1
Geometrical and microstructural characteristics of the cell components.

	Materials	Size [cm x cm]	Thickness [mm]	Porosity [%]
Fuel Electrode (FE)	Ni coated Al_2O_3	10.5 × 10.5	0.67	60
Oxygen Electrode (OE)	Lithiated NiO	11 × 11	0.70	65
Matrix	γ-$LiAlO_2$	13 × 13	1.19 (4 sheets)	60
Current Collector	Ni grid (at FE side) Steel grid (at OE side)	10.5 × 10.5 (FE) 11 × 11 (OE)	0.78 (FE and OE)	–

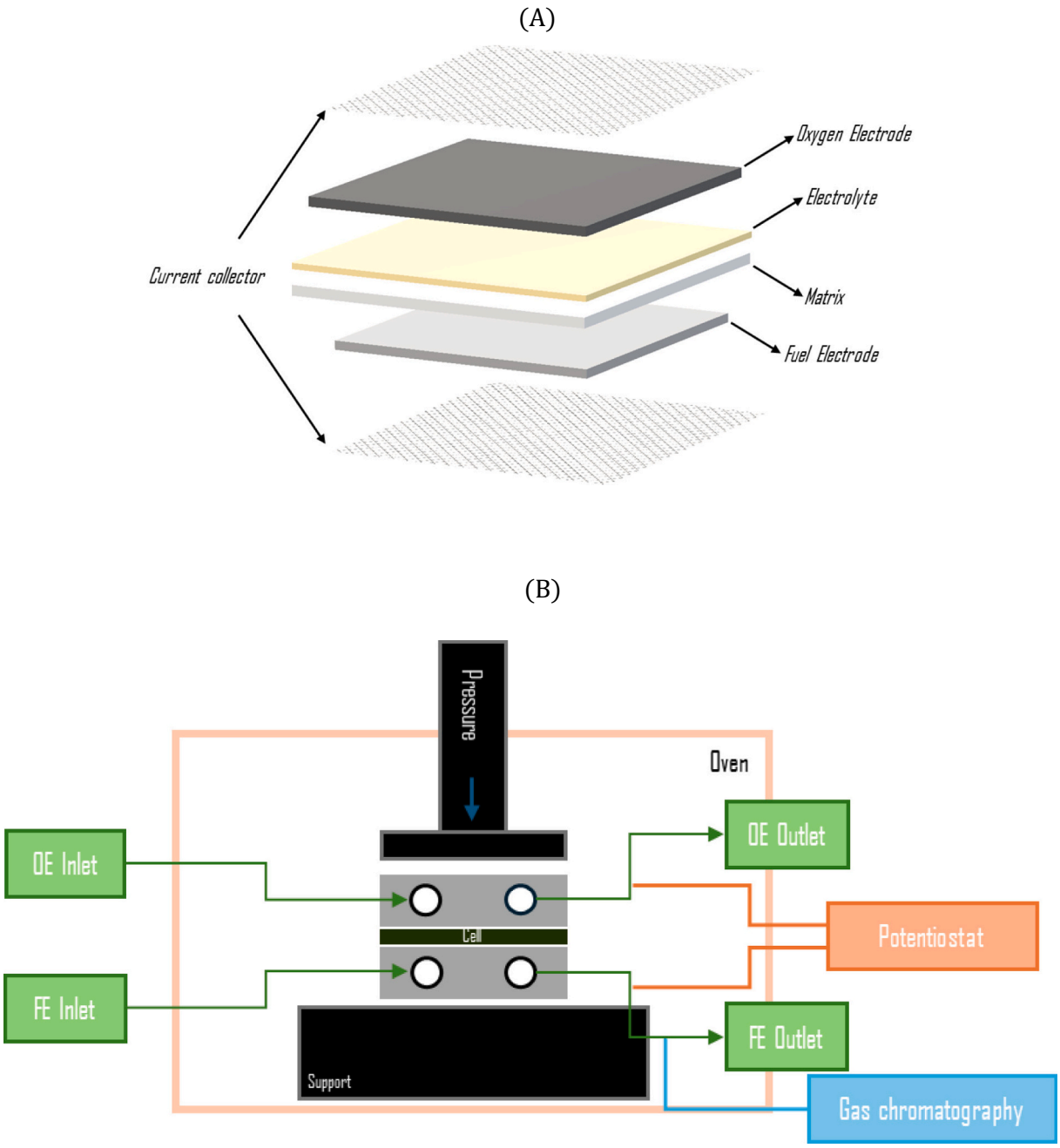

Fig. 2. Cell assembly (A) and frame connections (B).

Referring to diffusion and activation overpotentials ($\eta = \eta_c + \eta_a$), they represent voltage losses due to reaction development. These contributions derive from a kinetic approach that evaluates the redox reaction rate v_r dependent on the temperature through an Arrhenius-type formulation, the applied polarization and the species surface concentrations (the reduction is considered as the direct reaction in ***Eq. 8*-*Eq. 9***).

$$v_r = A'\exp\left(\frac{-E'_{act}}{RT}\right)\exp\left(\frac{-\beta_{red} z\eta F}{RT}\right)\prod C_{i,sur}^{\alpha'_i} - A''\exp\left(\frac{-E''_{act}}{RT}\right)\exp\left(\frac{\beta_{ox} z\eta F}{RT}\right)\prod C_{i,sur}^{\alpha''_i} \quad (8)$$

$$v_r = \gamma'\exp\left(\frac{-\beta_{red} z\eta F}{RT}\right)\prod C_{i,sur}^{\alpha'_i} - \gamma''\exp\left(\frac{\beta_{ox} z\eta F}{RT}\right)\prod C_{i,sur}^{\alpha''_i} \quad (9)$$

Where A' and A'' are the Arrhenius constants (direct and indirect reaction, respectively), E'_{act} and E''_{act} the activation energies (direct and indirect reaction, respectively), γ' and γ'' the kinetic constants (direct and indirect reaction, respectively), β_{red} and β_{ox} the charge transfer coefficients (direct and indirect reaction, respectively), η the electrode overpotential, α' and α'' the reaction orders of i-th component (direct and indirect reaction, respectively), C_{sur} the concentration at the active sites for the i-th component.

Applying Faraday law and multiplying/dividing the bulk concentration C_{bulk} at each term, the Butler-Volmer equation is obtained (***Eq. 10***) [54].

$$J = J_0\left[\exp\left(\frac{-\beta_{red} z\eta F}{RT}\right)\prod\frac{C_{i,sur}^{\alpha'_i}}{C_{i,bulk}^{\alpha'_i}} - \exp\left(\frac{\beta_{ox} z\eta F}{RT}\right)\prod\frac{C_{i,sur}^{\alpha''_i}}{C_{i,bulk}^{\alpha''_i}}\right] \quad (10)$$

Where J_O represents the exchange current density at the equilibrium

Table 2
Experimental test compositions for polarization curve measurements.

Sensitivity Analysis	–	Fuel Electrode	Oxygen Electrode
		$CO_2/H_2/H_2O/N_2$	$CO_2/N_2/O_2$
Reference composition [vol%] and flow rate [Nl h^{-1}]		33.0/33.0/34.0/– 54	30/55/15 57
H_2 study [vol%]	1	33.0/***11.0***/34.0/22.0	30/55/15
	2	33.0/***16.5***/34.0/16.5	
	3	33.0/***22.0***/34.0/11.0	
	4	33.0/***27.5***/34.0/5.5	
CO_2 study [vol%]	1	***11.0***/33.0/34.0/22.0	30/55/15
	2	***16.5***/33.0/34.0/16.5	
	3	***22.0***/33.0/34.0/11.0	
	4	***27.5***/33.0/34.0/5.5	
Flow rate study [Nl h^{-1}]	1	54	57
	2	70	
	3	80	
	4	90	

conditions (i.e., zero total current), which is equal for both directions of the reaction (***Eq. 11***).

$$J_0 = zF\gamma' \prod C_{i,bulk}^{\alpha_i'} = zF\gamma'' \prod C_{i,bulk}^{\alpha_i''} \tag{11}$$

Referring to molecular compounds or ions, their surface concentration depends on the transport from and to reaction sites. In a first approximation, it can be computed by solving interface balances at the electrode-electrolyte interface by assuming an infinitesimally thin active zone and applying Faraday's law for the reaction extent (***Eq. 12***-***Eq. 13***).

$$K_i\left(C_{i,sur} - C_{i,bulk}\right) = \nu_i \frac{|J|}{zF} \tag{12}$$

$$C_{i,sur} = C_{i,bulk} + \nu_i \frac{|J|}{zFK_i} \tag{13}$$

Where K is the material transport coefficient for the i-th component.

The concentration ratios in the Butler-Volmer equation (***Eq. 10***) can be simplified by substituting the surface concentration values by ***Eq. 13*** and introducing the limiting current density J_{LIM} for each i-th component by ***Eq. 14***. It is defined as the maximum current that is possible to have in an electrochemical process when the material transfer becomes the limiting phenomenon, permitting ***Eq. 15***.

$$J_{LIM,i} = zFK_iC_{i,bulk} \tag{14}$$

$$\frac{C_{i,sur}}{C_{i,bulk}} = 1 + \nu_i \frac{|J|}{J_{LIM,i}} \tag{15}$$

Therefore, the Butler-Volmer equation results in ***Eq. 16***.

$$J = J_0\left[\exp\left(\frac{-\beta_{red} z\eta F}{RT}\right)\prod\left(1+\nu_i'\frac{|J|}{J_{LIM,i}}\right)^{\alpha_i'} - \exp\left(\frac{\beta_{ox} z\eta F}{RT}\right)\prod\left(1+\nu_i''\frac{|J|}{J_{LIM,i}}\right)^{\alpha_i''}\right] \tag{16}$$

Where ν' and ν'' are the stoichiometric coefficients of the i-th component for the direct and indirect reactions, respectively.

Working far from the equilibrium conditions ($|J| \gg J_0$), the electrochemical reaction mainly occurs in one direction (reduction or oxidation) depending on the applied overpotential [55]. Here, the kinetics can be simplified by using the Tafel equation for irreversible electrode behaviour [56].

To analyse the cell performance based on these assumptions, it is essential to consider the reactions singularly and distinguish the electrode operation in fuel cell and electrolysis mode. The reduction process is characterised by a high negative overpotential ($\eta \ll 0$), the Butler-Volmer equation results in ***Eq. 17*** and ***Eq. 18***, where two terms are highlighted due to the diffusion and the activation losses (***Eq. 19***), respectively.

$$J = J_0\left[\exp\left(\frac{-\beta_{red} z\eta F}{RT}\right)\prod\left(1+\nu_i'\frac{|J|}{J_{LIM,i}}\right)^{\alpha_i'}\right] \tag{17}$$

$$\ln\left(\frac{J}{J_0}\right) = \frac{-\beta_{red} z\eta F}{RT} + \ln\prod\left(1+\nu_i'\frac{|J|}{J_{LIM,i}}\right)^{\alpha_i'} \tag{18}$$

$$\eta = \eta_c + \eta_a = \frac{RT}{\beta_{red} zF}\left[\ln\prod\left(1+\nu_i'\frac{|J|}{J_{LIM,i}}\right)^{\alpha_i'} + \ln\left(\frac{J_0}{J}\right)\right] \tag{19}$$

Whereas the oxidation process is characterised by a high positive overpotential ($\eta \gg 0$), resulting in the following formulations (***Eq. 20*** and ***Eq. 21***) where two contributions are again detected (***Eq. 22***). Note that the value of the current density should be negative in the case of an opposite reaction, according to the Butler-Volmer equation.

$$J = -J_0\left[\exp\left(\frac{\beta_{ox} z\eta F}{RT}\right)\prod\left(1+\nu_i''\frac{|J|}{J_{LIM,i}}\right)^{\alpha_i''}\right] \tag{20}$$

$$\ln\left(\frac{-J}{J_0}\right) = \frac{\beta_{ox} z\eta F}{RT} + \ln\prod\left(1+\nu_i''\frac{|J|}{J_{LIM,i}}\right)^{\alpha_i''} \tag{21}$$

$$\eta = \eta_c + \eta_a = \frac{RT}{\beta_{ox} zF}\left[-\ln\prod\left(1+\nu_i''\frac{|J|}{J_{LIM,i}}\right)^{\alpha_i''} + \ln\left(\frac{-J}{J_0}\right)\right] \tag{22}$$

It is noteworthy that, in a preliminary kinetic formulation, a negligible contribution of the activation overpotential in both directions can be considered due to the high working temperatures of molten carbonate cells [34,57,58].

3.1. Oxygen electrode kinetics

In literature, different reaction paths have been proposed for Ni oxide-based catalysts that depend on the used molten electrolyte (for example, Li—K and Li—Na) and consider both single electron charge transfer reactions and pure chemical reactions [59]. The two main mechanisms consist of the peroxide path, which has been verified for pure lithium and lithium-rich melts [60], and the superoxide path, which characterises sodium- and potassium-rich melts [61]. Such studies have focused on the oxygen reduction occurring under fuel cell mode (i.e., direct operation), but these same reaction paths have also been applied for the reverse reaction by assuming an equal rate-determining step [62,63]. It is noteworthy that literature has proposed possible alternatives under electrolysis cell operation, not identifying the same reactant composition dependences on the kinetics [64]. Nevertheless, further detailed analysis would be required for a better understanding. In view of the tested sample composed of $(Li_{0.62}K_{0.38})CO_3$, the peroxide path has been considered in the present work based also on previous observations of the authors [53]. It occurs according to ***Eq. 23***-***Eq. 24***-***Eq. 25***-***Eq. 26*** (considering the reduction as the direct reaction) [65].

$$\frac{1}{2}O_2 + CO_3^{2-} \leftrightarrow O_2^{2-} + CO_2 \tag{23}$$

$$O_2^{2-} + e^- \leftrightarrow O^{2-} + O^- \ (\text{rate} - \text{determining step}) \tag{24}$$

$$O^- + e^- \leftrightarrow O^{2-} \tag{25}$$

$$2CO_2 + 2O^{2-} \leftrightarrow 2CO_3^{2-} \tag{26}$$

Eq. 24 is assumed as the rate-determining step, while the others are considered equilibrium reactions [59]. With the aim of applying the Butler-Volmer equation to the rate-determining step of the peroxide path, ***Eq. 9*** results in the following formulation (***Eq. 27***) that considers the dependences of only reagent species and the stoichiometric coefficients as their reaction orders.

$$v_{r(OE)} = \gamma'_{(OE)}\exp\left(\frac{-\beta_{red(OE)}\eta_{(OE)}F}{RT}\right)C_{O_2^{2-},sur} - \gamma''_{(OE)}\exp\left(\frac{\beta_{ox(OE)}\eta_{(OE)}F}{RT}\right)C_{O^{2-},sur}C_{O^-,sur} \quad (27)$$

The reactant surface concentrations involved on the active sites can be computed assuming the equilibrium achievements for previous steps: O_2^{2-} are produced by ***Eq. 23*** under reduction (i.e., direct reaction), O^{2-} and O^- derive from ***Eq. 25*** and ***Eq. 26*** under oxidation (i.e., indirect reaction). Following this approach and assuming a fixed value for carbonate ions [66], ***Eq. 27*** can be rewritten as ***Eq. 28*** and ***Eq. 29*** [62].

$$v_{r(OE)} = cost'_{(OE)}\exp\left(\frac{-\beta_{red(OE)}\eta_{(OE)}F}{RT}\right)C_{O_2,sur}^{0.5}C_{CO_2,sur}^{-1} - cost''_{(OE)}\exp\left(\frac{\beta_{ox(OE)}\eta_{(OE)}F}{RT}\right)C_{CO_2,sur}^{-2} \quad (28)$$

$$J = J_{0(OE)}\left[\exp\left(\frac{-\beta_{red(OE)}\eta_{(OE)}F}{RT}\right)\frac{C_{O_2,sur}^{0.5}C_{CO_2,sur}^{-1}}{C_{O_2,bulk}^{0.5}C_{CO_2,bulk}^{-1}} - \exp\left(\frac{\beta_{ox(OE)}\eta_{(OE)}F}{RT}\right)\frac{C_{CO_2,sur}^{-2}}{C_{CO_2,bulk}^{-2}}\right] \quad (29)$$

The Butler-Volmer equation for the oxygen electrode in ***Eq. 29*** can be further simplified through interface balance resolution (***Eq. 12-Eq. 13***) since now only gaseous species are involved, as explained before. Introducing limiting current densities and assuming to work in the Tafel domain with negligible activation losses, the following equations characterise the oxygen electrode operation: ***Eq. 30*** considers the reduction in fuel cell mode according to ***Eq. 19***, and ***Eq. 31*** the oxidation in electrolysis mode according to ***Eq. 22***.

$$\eta_{c(OE)} = \frac{RT}{\beta_{red(OE)}F}\ln\left[\left(1-\frac{|J|}{2J_{LIM,O_2}}\right)^{0.5}\left(1-\frac{|J|}{J_{LIM,CO_2}}\right)^{-1}\right] \quad (30)$$

$$\eta_{c(OE)} = \frac{-RT}{\beta_{ox(OE)}F}\ln\left(1+\frac{|J|}{J_{LIM,CO_2}}\right)^{-2} \quad (31)$$

Where $\beta_{red(OE)}$ and $\beta_{ox(OE)}$ are equal to 0.5 and 1.5, respectively, in agreement with previous experimental observations [66] as well as theoretical correlations for the charge transfer coefficients as a function of total involved electrons and the number of occurrences of the rate-determining step [67].

3.2. Fuel electrode kinetics

Several paths have been proposed for the hydrogen evolution on nickel-based electrodes and have been validated in fuel cell mode, depending on the specific geometry and microstructure. Ang and Sammells presented the following reaction mechanism, consisting of one chemical reaction between hydrogen and the used metal M plus two in-series electrochemical reactions (***Eq. 32-Eq. 33-Eq. 34***), below identified as "Reaction Path 1" [68].

$$H_2 + 2M \leftrightarrow 2MH \quad (32)$$

$$MH + CO_3^{2-} \leftrightarrow OH^- + CO_2 + M + e^- \ (\text{rate}-\text{determining step}) \quad (33)$$

$$MH + OH^- \leftrightarrow H_2O + M + e^- \quad (34)$$

While Jewulski and Suski considered a similar approach but with a different occurrence of the rate-determining step in the hydrogen evolution reaction (***Eq. 35-Eq. 36-Eq. 37***), below identified as "Reaction Path 2" [69]. This reaction mechanism was also discussed in [70].

$$H_2 + 2M \leftrightarrow 2MH \quad (35)$$

$$2MH + 2CO_3^{2-} \leftrightarrow 2OH^- + 2CO_2 + 2M + 2e^- \ (\text{rate}-\text{determining step}) \quad (36)$$

$$2OH^- + CO_2 \leftrightarrow H_2O + CO_3^{2-} \quad (37)$$

Finally, Weewer, Hemmes, and Wit identified the first electrochemical reaction as the rate-determining step (***Eq. 38-Eq. 39-Eq. 40***), below defined as "Reaction Path 3" [71].

$$H_2 + CO_3^{2-} \leftrightarrow H_{ads} + OH^- + CO_2 + e^- \ (\text{rate}-\text{determining step}) \quad (38)$$

$$H_{ads} + CO_3^{2-} \leftrightarrow OH^- + CO_2 + e^- \quad (39)$$

$$2OH^- + CO_2 \leftrightarrow H_2O + CO_3^{2-} \quad (40)$$

As in the case of the oxygen electrode, the equation (***Eq. 9***) can be applied to the rate-determining step of each reaction path, considering the dependences of only reagent species and the stoichiometric coefficients as their reaction orders. In all proposed mechanisms, a single charge transfer reaction step has to be considered, assuming an equal limiting step in both the direct and the indirect reaction (***Eq. 41-Eq. 42-Eq. 43***). It is noteworthy that reaction orders α, kinetic coefficients γ and charge transfer coefficients β depend on the specifically applied reaction path among the three cases.

- Reaction Path 1 (RP1)

$$v_{r(FE)} = \gamma'^{RP1}_{(FE)}\exp\left(\frac{-\beta^{RP1}_{red(FE)}\eta_{(FE)}F}{RT}\right)C_{OH^-,sur}C_{CO_2,sur}$$

$$-\gamma''^{RP1}_{(FE)}\exp\left(\frac{\beta^{RP1}_{ox(FE)}\eta_{(FE)}F}{RT}\right)C_{CO_3^{2-},sur}C_{MH,sur} \quad (41)$$

- Reaction Path 2 (RP2)

$$v_{r(FE)} = \gamma'^{RP2}_{(FE)}\exp\left(\frac{-\beta^{RP2}_{red(FE)}\eta_{(FE)}F}{RT}\right)C_{OH^-,sur}C_{CO_2,sur}$$

$$-\gamma''^{RP2}_{(FE)}\exp\left(\frac{\beta^{RP2}_{ox(FE)}\eta_{(FE)}F}{RT}\right)C_{CO_3^{2-},sur}C_{MH,sur} \quad (42)$$

- Reaction Path 3 (RP3)

$$v_{r(FE)} = \gamma'^{RP3}_{(FE)}\exp\left(\frac{-\beta^{RP3}_{red(FE)}\eta_{(FE)}F}{RT}\right)C_{OH^-,sur}C_{CO_2,sur}C_{H_{ads},sur} - \gamma''^{RP3}_{(FE)}\exp\left(\frac{\beta^{RP3}_{ox(FE)}\eta_{(FE)}F}{RT}\right)C_{CO_3^{2-},sur}C_{H_2,sur} \quad (43)$$

The surface concentration values can be computed assuming the equilibrium achievement for previous steps and a fixed value for carbonate ion concentration [66]. Under reduction (i.e., direct reaction), OH^- ions are produced by ***Eq. 34*** in Reaction Path 1 and by ***Eq. 37*** in Reaction Path 2, OH^- ions and H_{ads} by ***Eq. 39-Eq. 40*** in Reaction Path 3.

Under oxidation (i.e., indirect reaction), *MH* derives from ***Eq. 32*** in Reaction Path 1 and ***Eq. 35*** in Reaction Path 2. The Butler-Volmer equation for the fuel electrode results in ***Eq. 44*** (reduction as the direct reaction and oxidation as the inverse one), where exchange current density, the reaction orders α and the charge transfer coefficients β vary with the applied reaction path as reported in Table 3.

$$J = J^{j}_{0(FE)}\left[\exp\left(\frac{-\beta^{j}_{red(FE)}\eta_{(FE)}F}{RT}\right)\frac{C^{\alpha'^{j}_{H_2}}_{H_2,sur}C^{\alpha'^{j}_{H_2O}}_{H_2O,sur}C^{\alpha'^{j}_{CO_2}}_{CO_2,sur}}{C^{\alpha'^{j}_{H_2}}_{H_2,bulk}C^{\alpha'^{j}_{H_2O}}_{H_2O,bulk}C^{\alpha'^{j}_{CO_2}}_{CO_2,bulk}} - \exp\left(\frac{\beta^{j}_{ox(FE)}\eta_{(FE)}F}{RT}\right)\frac{C^{\alpha''^{j}_{H_2}}_{H_2,sur}}{C^{\alpha''^{j}_{H_2}}_{H_2bulk}}\right] \text{ with } j = RP1, RP2, RP3 \quad (44)$$

Interface material balances allow for computing the surface concentrations of gaseous reactants in ***Eq. 44***. Introducing then their limiting current densities and assuming to work in the Tafel domain with negligible activation losses, the following equations characterise the fuel electrode operation in electrolysis mode (reduction according to ***Eq. 45***) and in fuel cell mode (oxidation according to ***Eq. 46***).

$$\eta_{c(FE)} = \frac{RT}{\beta^{j}_{red(FE)}F}\ln\left[\left(1+\frac{|J|}{J_{LIM,H_2}}\right)^{\alpha'^{j}_{H_2}}\left(1-\frac{|J|}{J_{LIM,H_2O}}\right)^{\alpha'^{j}_{H_2O}}\left(1-\frac{|J|}{J_{LIM,CO_2}}\right)^{\alpha'^{j}_{CO_2}}\right] \text{ with } j = RP1, RP2, RP3 \quad (45)$$

$$\eta_{c(FE)} = \frac{-RT}{\beta^{j}_{ox(FE)}F}\ln\left(1-\frac{|J|}{J_{LIM,H_2}}\right)^{\alpha''^{j}_{H_2}} \text{ with } j = RP1, RP2, RP3 \quad (46)$$

Refer to **Fig. S.1** in Supplementary Material, which represents a flowchart summarising the formulation of electrode polarization losses from the Butler-Volmer equation.

Assuming ideal gas behaviour at atmospheric working pressure with negligible pressure drops and isothermal cell operation, the bulk concentrations/partial pressures of gaseous reactants applied in the limiting current density definition and Nernst equation derive from macroscopic material balances that allow for computing an average composition between inlet and outlet values. Here, the model provides a preliminary evaluation of the concentration gradients both along the electrode thickness due to reaction development through interface balances (***Eq. 12***-***Eq. 13***) and on the cell plane due to an uneven gas distribution in a co-flow feeding configuration (***Eq. 47***) [53,56]. In the macroscopic material balances, the electrochemical reaction extent is computed through Faraday's law (***Eq. 48***) [56], while WGS is considered an equilibrium reaction (***Eq. 49***) [72].

$$N_{i,in} - N_{i,out} + \nu^{EL}_{i}X^{EL} + \nu^{WGS}_{i}X^{WGS} = 0 \quad (47)$$

$$X^{EL} = \frac{|J|S}{zF} \quad (48)$$

$$K^{WGS}_{eq} = \frac{P_{H_2}P_{CO_2}}{P_{H_2O}P_{CO}} = \exp\left(\frac{-\Delta G^{WGS}}{RT}\right) \quad (49)$$

Where N is the molar flow rate of i-th component at the inlet "*in*" and the outlet "*out*", ν the stoichiometric coefficient of i-th component according to ***Eq. 2***, ***Eq. 3*** and ***Eq. 4***, X the reaction extent, referring to the electrochemical "*EL*" and the water gas shift reaction "*WGS*" reaction, respectively, S the active area, K^{WGS}_{eq} the WGS equilibrium constant and ΔG^{WGS} the WGS Gibbs free energy variation.

Moreover, the transport coefficient in the interface material balances (***Eq. 12***) can be computed by considering a Fickian-type diffusion of gaseous reactants within the porous electrodes (***Eq. 50***).

$$\frac{\mathscr{D}_{i,mix}\left(C_{i,sur} - C_{i,bulk}\right)}{d} = \nu_i\frac{|J|}{zF} \quad (50)$$

Where $\mathscr{D}_{mix}$ is the diffusive coefficient of i-th component in the gas mixture and d the electrode thickness. The molecular diffusivity is computed for a gas binary mixture on the basis of diffusion coefficient $\mathscr{D}_{i,j}$ (***Eq. 51***) and then is weighted on molar fractions y of the i-th component (***Eq. 52***) [73,74].

$$\mathscr{D}_{i,j}\left[\frac{cm^2}{s}\right] = \frac{0.00143\,T[K]^{1.75}}{P[atm]\left(\frac{2}{\frac{1}{M_i}+\frac{1}{M_j}}\right)^{0.5}\left(w_i^{\frac{1}{3}}+w_j^{\frac{1}{3}}\right)^2} \quad (51)$$

$$\mathscr{D}_{i,mix} = \frac{\varepsilon}{\tau}\left(\sum_{i\neq j}\frac{y_j}{\mathscr{D}_{i,j}}\right)^{-1}(1-y_i) \quad (52)$$

Where M_i and M_j are the molecular weights, w_i and w_j the atomic diffusion volumes of the i-th component and the j-th component of the mixture, respectively, ε the electrode porosity and τ the electrode tortuosity.

4. Results

Reversible operation of molten carbonate cells was investigated by an electrochemical characterization, where experimental observations at common working conditions were the basis for a preliminary validation of the proposed kinetic model. The study allowed for identifying the main polarization losses of each mode and correlating them with fed gas compositions at the fuel electrode.

In detail, referring to the cell testing, the polarization curve measurements led to detecting the main effects of the working conditions on the cell kinetics. Before starting the electrochemical characterization by varying operation parameters as reported in Table 2, EIS analysis allowed for checking an acceptable adhesion among layers and carbonate melting within the porous structure. As an example, Fig. 3 shows the spectra at 600 °C recorded during the controlled temperature initial ramp. As evident from the spectrum, the performance was quite satisfactory, with an internal resistance and a polarization resistance of approximately 0.8 Ω cm^2 and 2.2 Ω cm^2, respectively.

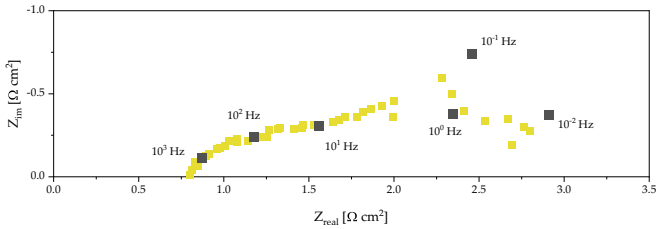

Fig. 3. Nyquist plot @ 600 °C – 18/72/10 vol% of $CO_2/H_2/H_2O$ and 30/55/15 vol% of $CO_2/N_2/O_2$ -reference flow rates- OCV condition (observed scattering due to possible connection-related issues).

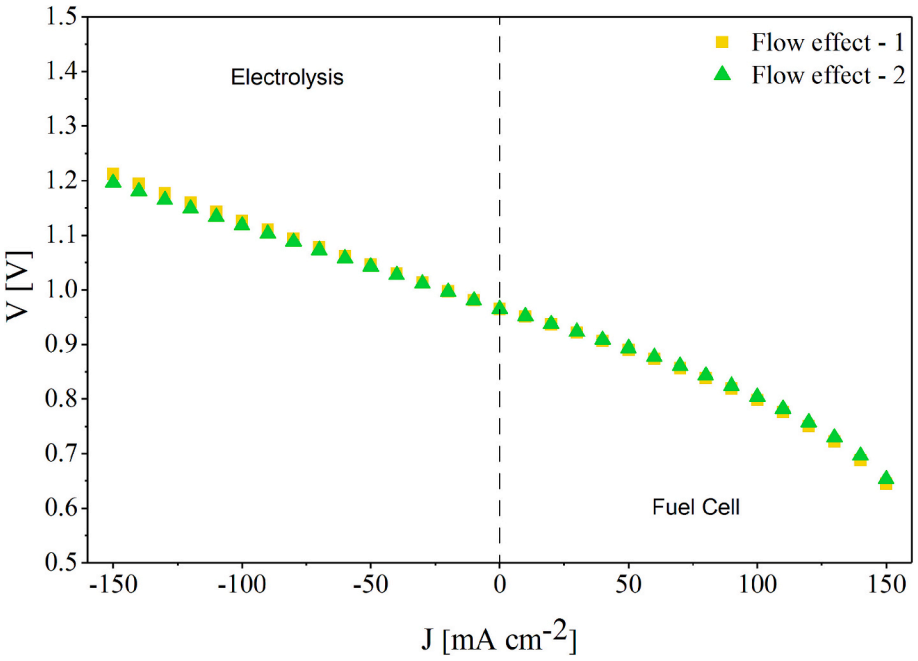

Fig. 4. Polarization curves @ 650 °C – 22/22/34/22 vol% of $CO_2/H_2/H_2O/N_2$ and 30/55/15 vol% of $CO_2/N_2/O_2$ – variable flow rates at the fuel electrode (refer to the first two cases at equal gas composition shown in Table 2 among "Flow rate study").

According to polarization curve measurements at 650 °C, the correlation between cell voltage and fuel electrode flow rate was first evaluated. Based on the results in Fig. 4 comparing curves at equal gas compositions and variable flow rates, the close overlap suggests that the applied conditions were far enough from the limiting currents, resulting in reactant utilizations lower than 35 %.

Other tests focused on fuel composition effects by varying the fed fraction of hydrogen and carbon dioxide at the fuel electrode, as shown in Table 2. Each test was performed in both modes, fuel cell and electrolysis, with the aim of evaluating the performance change under a reversible operation at equal gas supply. Analysing the hydrogen effect (Fig. 5.**A**), when its content is reduced, the fuel cell voltage has a drastic decrease due to possible reactant starvation and lower equilibrium voltages. Under electrolysis operation, indirect effects on gas transport should occur since water and carbon dioxide are the limiting reactants. Increasing the hydrogen content results in higher cell voltages until around 30 vol% H_2, beyond that, the electrolyser voltage reduces again. These experimental observations partially agree with [51], where a reduced hydrogen amount favours the operation up to 120 mA cm^{-2}. Whereas, according to [52], a negligible effect should occur on the polarization losses mainly affecting the OCV value, but hydrogen contents higher than 50 vol% H_2 were considered in these tests. As expected from the analysis of similar literature results [40,52], in electrolysis mode, the increasing amount of carbon dioxide at the fuel electrode side provokes a reduction in the cell voltage by favouring the reaction development (Fig. 5.**B**). Differently, the influence on the fuel cell operation is less marked, as observed in [51] for a reversible cell. These trends partially confirm the reference reaction paths in fuel cell mode, which propose a direct dependence just on the hydrogen supply (***Eq. 46***). Moreover, IV curve linear profile at low currents in both modes confirms the model assumption of a negligible contribution of activation losses, as already observed in [34,58].

Starting from the theoretical formulation presented in the third paragraph, experimental data fitting allowed for model tuning and identification of the unknown parameters. An empirical parameter λ was introduced to account for the non-directly measurable microstructural features of the electrode, such as effective porosities after electrolyte melting and tortuosity. Interface material balances for gas species (***Eq. 50***) were reformulated as ***Eq. 53*** with the consequent limiting current density J_{LIM} to apply in the diffusion overpotential (***Eq. 54***).

$$\lambda \mathscr{D}^{*}_{i,mix}\left(C_{i,sur} - C_{i,bulk}\right) = \nu_i \frac{|J|}{zF} \tag{53}$$

$$J_{LIM,i} = zF\lambda \mathscr{D}^{*}_{i,mix} C_{i,bulk} \tag{54}$$

In this last equation, λ is a fitting parameter specific to each electrode that incorporates information related to its microstructure (i.e., porosity, tortuosity and thickness), and $\mathscr{D}^{*}_{i,mix}$ is the diffusion coefficient of the *i*-th component in the mixture without considering such microstructural parameters.

Referring to the reaction orders, they were defined at the oxygen electrode following the peroxide reaction path (***Eq. 30***-***Eq. 31***). While three proposed mechanisms were tested for the fuel electrode, using values reported in Table 3. An additional fitting parameter λ_{OCV} was added to consider a constant bias of the open circuit voltage with respect to values predicted by the Nernst equation (***Eq. 6***). This overestimation has also been reported in the previous literature and may be due to cell working issues, such as leakages and/or material corrosion [75]. Referring to the ohmic resistance R_Ω, it was computed according to internal resistance measurements from EIS and by evaluating an activation energy for the cell conductivity of 0.32 eV.

In Table 4 the fitting parameters and simulation errors are reported for the three proposed reaction paths at the fuel electrode, observing quite similar results with the lowest value in the case of Reaction Path 2 proposed by Jewulski and Suski [69]. Minimum influence of the reaction path choice on model predictions suggests a low dependence of the fuel electrode reaction orders within the considered working conditions. Indeed, the main difference results in Reaction Path 1 under a reduction process where hydrogen order is not zero. Nevertheless, its limiting current densities are still high, confirming an indirect dependence of the hydrogen content, as discussed following. Since the kinetic model is not a deciding factor, in the following, the analysis is just presented for Reaction Path 2 that was taken as the reference.

Fig. 6.**A** compares the experimental values with the simulated ones in the case of Reaction Path 2. According to the residual plot (Fig. 6.**B**), a high discrepancy is visible at low voltages (i.e., the material transfer

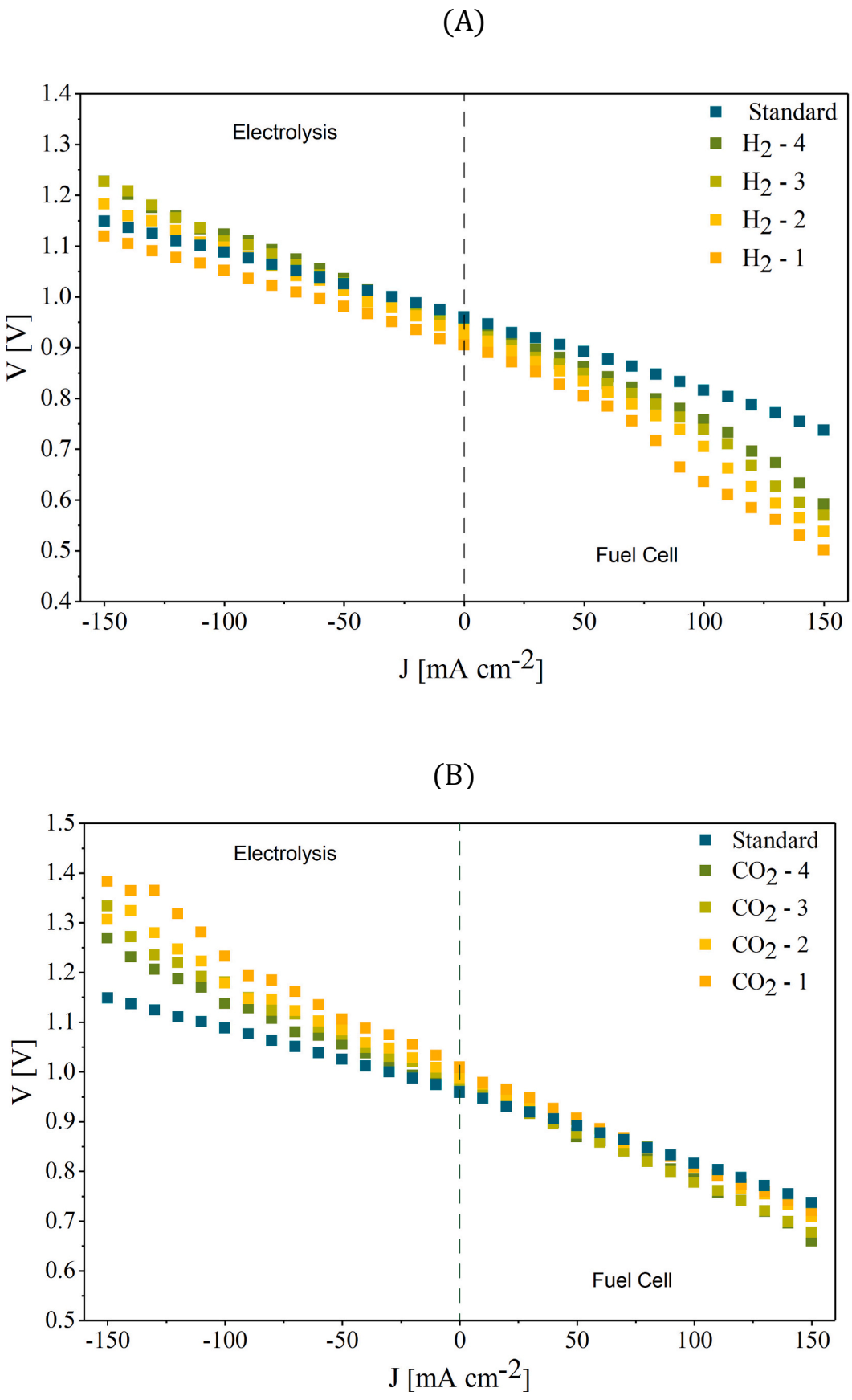

Fig. 5. Polarization curves @ 650 °C – variable H_2 (A) and CO_2 (B) compositions at the fuel electrode – reference gas composition at the oxygen electrode – reference flow rates (refer to "CO_2 and H_2 study" in Table 2).

Table 3
Kinetic parameters for the fuel electrode referring to three reaction paths [68,70,71].

Parameter	Reaction Path 1	Reaction Path 2	Reaction Path 3
α'_{H_2}	−0.5	0	0
α'_{H_2O}	1	0.5	1
α'_{CO_2}	1	0.5	1
α''_{H_2}	0.5	0.5	1
$\beta_{red(FE)}$	1.5	0.5	1.5
$\beta_{ox(FE)}$	0.5	0.5	0.5

Table 4
Fitting parameters with relative errors between measured and simulated cell voltage applying three reaction paths at the fuel electrode.

Parameter	Reaction Path 1	Reaction Path 2	Reaction Path 3
λ_{OCV} [V]	−0.006	−0.010	−0.005
λ_{FE} [cm^{-1}]	0.50	0.50	0.50
λ_{OE} [cm^{-1}]	0.58	0.59	0.59
Error [%]	3.3	3.0	3.2

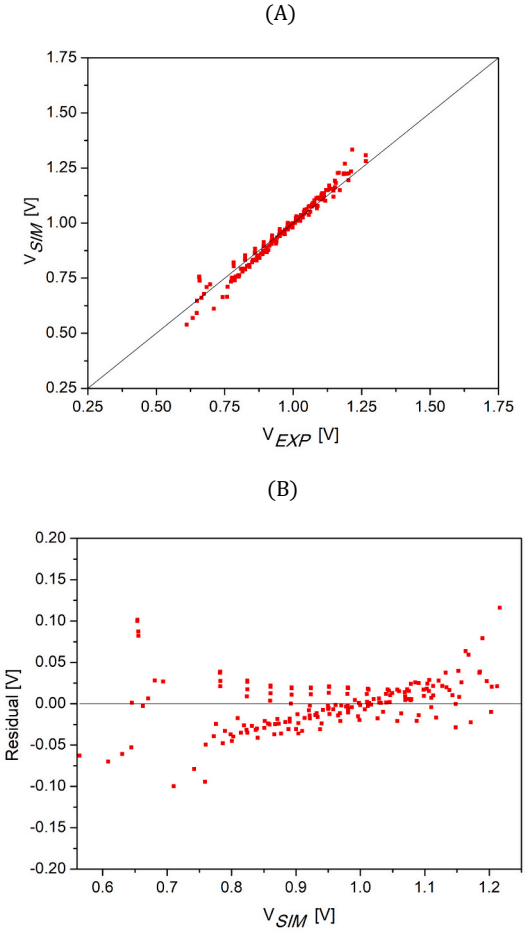

Fig. 6. Comparison between experimental data and simulated cell voltages at variable working conditions (A) and residual plot (B), assuming Reaction Path 2 as the fuel electrode kinetics.

regime for some fed compositions), where simplified interface balances may fail to describe the gas effective diffusion, requiring local modelling to increase the simulation accuracy.

A sensitivity analysis was also performed to evaluate the influence of

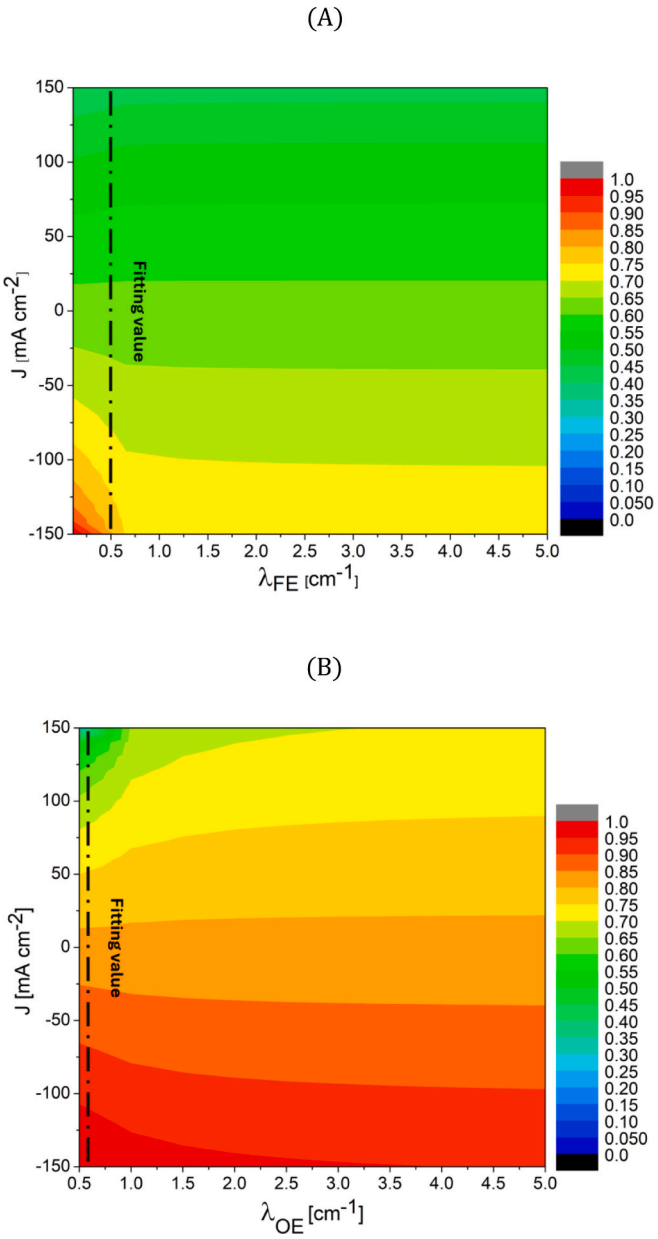

Fig. 7. Sensitivity analysis on the influence of fitting parameters correlated to electrode microstructure on the normalised voltage of the reversible cell in the case of the fuel electrode (A) and the oxygen electrode (B) @ 650 °C – reference gas compositions – reference flow rates. Refer to **Fig. S.2** for the raw data.

fitting parameters (λ), correlated to microstructural features, on the cell performance. λ_{FE} and λ_{OE} were varied in the ranges to maintain a physical meaning. Fig. 7 shows how the normalised voltage of the reversible cell changes as a function of the applied current density. The performance prediction is little influenced at increasing λ values (i.e., higher porosity, lower tortuosity and thickness). In other words, further improvements on microstructural parameters do not lead to a visible operation optimization. This is valid for both fuel and oxygen electrode parameters, since the variation is mainly correlated to the applied currents. A drastic increase is only present at a low λ_{FE} in electrolysis mode, where the fuel electrode loss becomes the predominant contribution due to CO_2 and H_2O diffusion issues.

The developed model allowed a preliminary investigation of the weight of different overpotentials under reversible cell behaviour, distinguishing ohmic losses, fuel electrode losses and oxygen electrode losses (***Eq. 5***). The contributions in electrolysis and fuel cell mode at

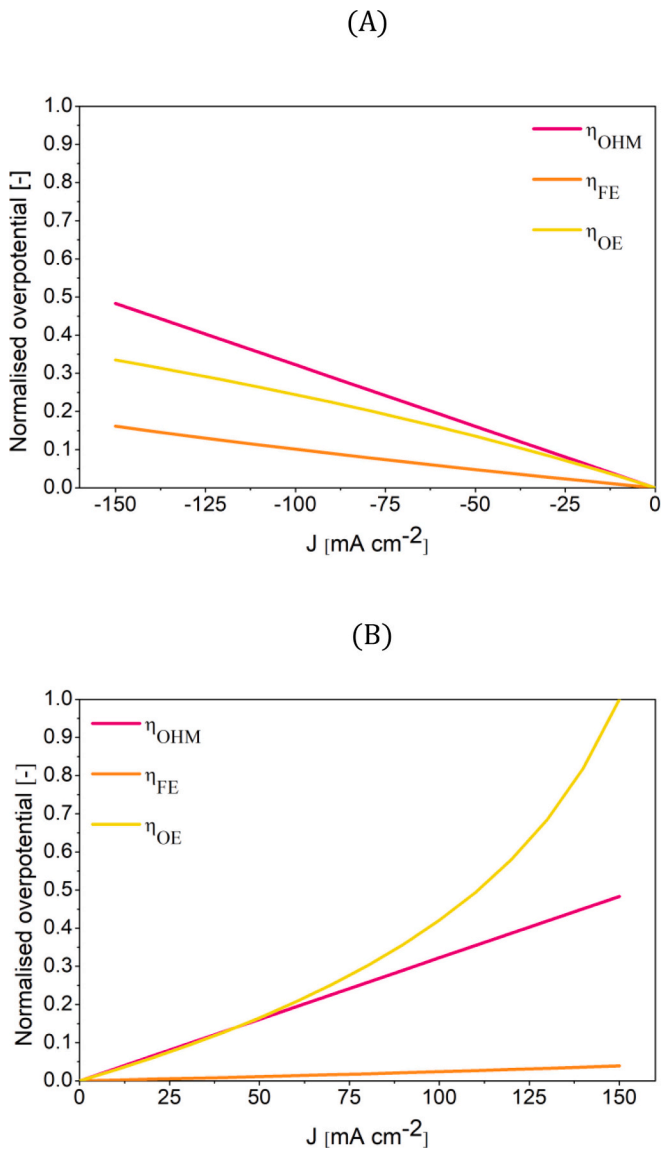

Fig. 8. Simulated polarization losses using normalised values @ 650 °C – reference gas compositions – reference flow rates in the case of (A) electrolysis and (B) fuel cell operation (note that absolute values of polarization losses are plotted for graphical reasons). Refer to **Fig. S.3** for the raw data.

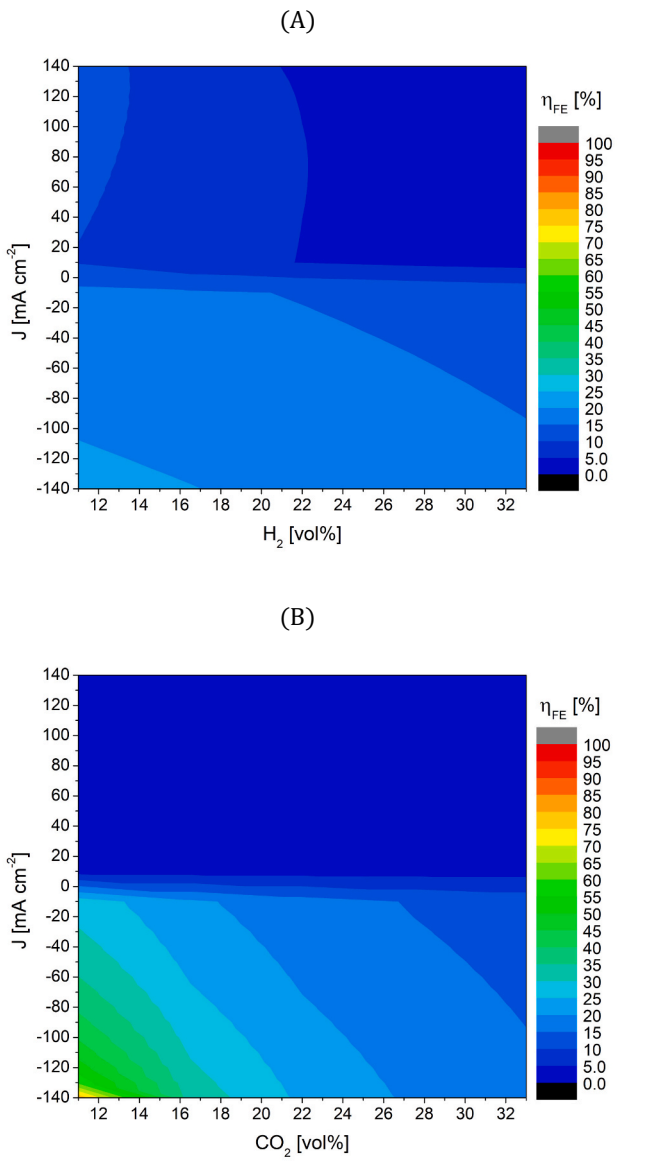

Fig. 9. Percentage contribution of the fuel electrode loss on cell total polarization loss varying applied currents and fed compositions in terms of H_2 (A) and CO_2 (B) @ 650 °C – reference gas compositions at the oxygen electrode – reference flow rates.

reference conditions are presented in Fig. 8 in terms of normalised values and in **Fig. S.3** for raw data. An asymmetrical behaviour is underlined. Indeed, looking at the ohmic overpotential that is equal in both by depending just on the temperature, it results in the main loss in electrolysis operation, while the oxygen electrode loss is higher under a fuel cell mode. In all working points, the overpotential contribution of the oxygen electrode is higher than that of the fuel electrode. This finding is consistent with the literature [76] and is attributed to a slower kinetics of the oxygen evolution reaction. Moreover, also considering the gas diffusivity, the hydrogen and water transport from and to the electrolyte interface within the fuel electrode is easier due to small molecular sizes, resulting in higher limiting current densities (up to ten times with respect to O_2 and CO_2 values at the oxygen electrode). Comparing the oxygen electrode profiles in the two operating modes, the sharp increase of the overpotential loss under fuel cell mode is due to the reactant amount reduction, while in electrolysis mode the product accumulation results in milder effects. Referring to the fuel electrode, an opposite trend is visible: a higher contribution characterises the electrolysis mode, where the water and carbon dioxide have a higher limiting current density with respect to hydrogen in fuel cell mode.

Referring to the effects of the fuel electrode feed composition (Fig. 9 and **Fig. S.4**), high overpotentials refer to the electrolysis mode at each considered feed. In more detail, in the case of hydrogen variation (**Fig. S.4.A** and **Fig. S.4.B**), the highest values were observed at the lowest hydrogen concentrations and the highest tested currents in both modes. Indeed, working as a fuel cell, the hydrogen depletion increases the diffusion overpotential by reducing the H_2 limiting current density from ~1730 mA cm^{-2} at 33 vol% H_2 to ~400 mA cm^{-2} at 11 vol% H_2. However, considering a working range up to 140 mA cm^{-2}, the fuel electrode loss contribution is still lower (~10 %) with respect to the cell total polarization loss (Fig. 9.**A**). Referring to Reaction Path 2, there is not a direct dependence on hydrogen in electrolysis mode (i.e., the H_2 reaction order is equal to zero), but the diffusion mechanism of all involved gases changes. Indeed, both water and carbon dioxide limiting current densities increase at high hydrogen content since the reactant diffusion is favoured in a hydrogen-rich mixture in view of its low molecular size, in agreement with ***Eq. 51***. Moreover, in the case of high

hydrogen content, the feed is not diluted by nitrogen and here the water composition averaged on the cell plane is higher, further favouring the kinetics. Accordingly, the fuel electrode loss percentage slightly decreases, resulting in around ~21 % vs. ~16 % at −140 mA cm^{-2}, 11 vol % and 33 vol% H_2, respectively (Fig. 9**.A**). This preliminary observation would suggest the usefulness of recycling a fraction of produced hydrogen to favour the reaction kinetics in electrolysis mode, in addition to avoiding the electrode oxidation.

For the carbon dioxide variations (**Fig. S.4.C** and **Fig. S.4.D**), higher polarization losses characterise high applied currents, reaching the maximum in electrolysis. The fuel cell overpotential remains almost constant (**Fig. S.4.C**) in agreement with reference reaction paths, which consider hydrogen content as the main factor (in these tests set at 33 vol %, meaning low losses). A minimum increase was actually measured at higher CO_2 contents that slightly penalise hydrogen diffusion, resulting in a hydrogen limiting current density of ~1730 mA cm^{-2} at 33 vol% CO_2 and 1860 mA cm^{-2} at 11 vol% CO_2. Referring to the fuel electrode contribution to the total polarization loss (Fig. 9**.B**), no variation is visible, resulting in a value of ~3 %. In electrolysis mode (**Fig. S.4.D**), the fuel electrode overpotential increases as the CO_2 concentration decreases due to possible starvation. Indeed, the CO_2 limiting current density varies from ~700 mA cm^{-2} at 33 vol% CO_2 to lower than 150 A cm^{-2} at 11 vol% CO_2, as confirmed by the exponential curve increase in Fig. 5**.B**. With CO_2 becoming the limiting reactant in electrolysis, a drastic increase of the losses up to ~80 % is visible in the case of 11 vol% CO_2 (Fig. 9**.B**).

5. Conclusions

The aim of this work was the electrochemical characterization of reversible molten carbonate cell operation. A lab test campaign was performed to analyse the behaviour at varying working conditions, with a more specific focus on the fuel electrode feed. Based on the reference reaction paths for each electrode, a kinetic model capable of predicting both fuel cell and electrolysis operation modes was then developed and preliminarily validated on experimental data, achieving on average a relative error of approximately 3 %.

Peculiarities of each polarization loss in both fuel cell and electrolysis were evaluated. Generally, the oxygen electrode provides the main contribution to the polarization losses due to slower kinetics. Nevertheless, the fuel electrode shows the highest weight in the electrolysis mode at low CO_2 levels, underlining one of the possible challenges of reversible cell management.

Looking at the fuel electrode investigation, hydrogen content has the predominant influence on the fuel cell kinetics, while fed CO_2 characterises the electrolysis operation. The fuel electrode overpotential decreases at high hydrogen concentrations since starvation is avoided in fuel cell mode and the reactant diffusion is favoured in hydrogen-rich mixtures in electrolysis mode, showing an H_2 indirect effect on the reaction development. The cell exhibits an asymmetric behaviour according to the concentration of CO_2 at the fuel electrode: negligible variations in fuel cell mode occur when changing the CO_2 content, while in electrolysis mode the CO_2 reduction causes an exponential increase in the resistance.

It is noteworthy that the presented results provide a preliminary interpretation of occurring phenomena in a reversible molten carbonate cell, using simplified lumped parameter modelling. More detailed observations could be achieved by widening the ranges considered of the working conditions with a focus on temperature, oxygen electrode feed and water composition at the fuel electrode. Moreover, multidimensional models, solving conservation equations in the electrode volume, could provide a detailed evaluation of different occurring phenomena, such as gas diffusion, charge preferential paths, uneven catalytic activity and so on. This would permit a finer calculation of reactant concentration gradients along the electrode thicknesses and, here, a better estimation of the diffusion overpotentials that are the main losses in high-temperature cells.

CRediT authorship contribution statement

Lucia Cardona: Writing – review & editing, Writing – original draft, Visualization, Validation, Software, Methodology, Investigation, Conceptualization. **Fiammetta Rita Bianchi:** Writing – review & editing, Writing – original draft, Visualization, Software, Methodology. **Emilio Audasso:** Writing – review & editing, Validation, Investigation, Conceptualization. **Dario Bove:** Writing – review & editing, Supervision, Conceptualization. **Sung Pil Yoon:** Supervision, Project administration. **Barbara Bosio:** Writing – review & editing, Supervision, Project administration, Conceptualization.

Funding

This research was partially developed within the project “Network 4 Energy Sustainable Transition – NEST” funded under the National Recovery and Resilience Plan (NRRP), Mission 4 Component 2 Investment 1.3 - Call for tender No. 1561 of 11.10.2022 of Ministero dell’Università e della Ricerca (MUR); funded by the European Union – NextGenerationEU. Moreover, it was partially supported by the Energy Technology Program of the Korea Institute of Energy Technology Evaluation and Planning (KETEP), granted resources from the Ministry of Trade, Industry & Energy, Republic of Korea (No. 20213030040080) and financially supported by the KIST institutional program for the Korea Institute of Science and Technology (No. 2E32592).

Declaration of competing interest

The authors declare that they have no known competing financial interests or personal relationships that could have appeared to influence the work reported in this paper.

Appendix A. Supplementary data

Supplementary data to this article can be found online at https://doi.org/10.1016/j.elecom.2025.108023.

Data availability

The data that has been used is confidential.

References

[1] A. Mehmeti, F. Santoni, M. Della Pietra, S.J. McPhail, Life cycle assessment of molten carbonate fuel cells: state of the art and strategies for the future, J. Power Sources 308 (2016) 97–108, https://doi.org/10.1016/j.jpowsour.2015.12.023.
[2] D. Bove, E. Audasso, T. Barckholtz, G. Kiss, J. Rosen, B. Bosio, Process analysis of molten carbonate fuel cells in carbon capture applications, Int. J. Hydrogen Energy 46 (2021) 15032–15045, https://doi.org/10.1016/j.ijhydene.2020.08.020.
[3] J. Yazdanfar, M. Mehrpooya, H. Yousefi, A. Palizdar, Energy and exergy analysis and optimal design of the hybrid molten carbonate fuel cell power plant and carbon dioxide capturing process, Energ. Conver. Manage. 98 (2015) 15–27, https://doi.org/10.1016/j.enconman.2015.03.076.
[4] N. Kousheshi, A. Nouri, A. Chitsaz, A. Saberi, Comparative study of CO_2 capture strategies in optimized MCFC-based power systems : Performance, cost, and environmental perspectives, J. CO2 Util. 95 (2025) 103085, https://doi.org/10.1016/j.jcou.2025.103085.
[5] H. Luo, F. Cheng, T.A. Barckholtz, C. Greig, E.D. Larson, Biopower with molten carbonate fuel cell carbon dioxide capture: performance, cost, and grid-integration evaluations, Energ. Conver. Manage. 322 (2024) 119167, https://doi.org/10.1016/j.enconman.2024.119167.

[6] S. Ferguson, A. Tarrant, Molten carbonate fuel cells for 90% post combustion CO_2 capture from a new build CCGT, Front. Energy Res. 9 (2021) 1–6, https://doi.org/10.3389/fenrg.2021.668431.
[7] M.A. Abdelkareem, M.A. Lootah, E.T. Sayed, T. Wilberforce, H. Alawadhi, B.A. A. Yousef, A.G. Olabi, Fuel cells for carbon capture applications, Sci. Total Environ. 769 (2021) 144243, https://doi.org/10.1016/j.scitotenv.2020.144243.
[8] The fuel cell industry review 2012, Platin. Met. Rev. 56 (2012) 272–273, https://doi.org/10.1595/147106712x657535.
[9] I. Rexed, M. Della Pietra, S. McPhail, G. Lindbergh, C. Lagergren, Molten carbonate fuel cells for CO_2 separation and segregation by retrofitting existing plants - an analysis of feasible operating windows and first experimental findings, Int. J. Greenh. Gas Control. 35 (2015) 120–130, https://doi.org/10.1016/j.ijggc.2015.01.012.
[10] M.G. Kang, C.W. Lee, H.S. Dong, S.C. Jang, S.A. Song, H.S. Park, S.H. Choi, H. C. Ham, J. Han, S.W. Nam, S.H. Kim, S.P. Yoon, Effects of vibrations in marine environments on performance of molten-carbonate fuel cells, Int. J. Hydrogen Energy 41 (2016) 18732–18738, https://doi.org/10.1016/j.ijhydene.2016.02.134.
[11] K.I. Kim, J.K. Bae, E. Audasso, A.W. Cho, Y.B. Jun, H.S. Park, S.C. Jang, Y.S. Cho, H.S. Kim, S.H. Choi, S.P. Yoon, In situ electrolyte replenishment with atmospheric pressure-chemical/electrochemical vapour deposition for molten carbonate fuel cells, Chem. Eng. J. 476 (2023) 146663, https://doi.org/10.1016/j.cej.2023.146663.
[12] J. Milewski, W. Bujalski, M. Wołowicz, K. Futyma, J. Kucowski, R. Bernat, Experimental investigation of CO_2 separation from lignite flue gases by 100 cm^2 single molten carbonate fuel cell, Int. J. Hydrogen Energy 39 (2014) 1558–1563, https://doi.org/10.1016/j.ijhydene.2013.08.144.
[13] Ship Technology, Viking Lady, Available online, https://www.ship-technology.com/projects/viking-lady/ (accessed on 8 May 2025).
[14] S. Valluri, V. Claremboux, S. Kawatra, Opportunities and challenges in CO_2 utilization, J. Environ. Sci. (China) 113 (2022) 322–344, https://doi.org/10.1016/j.jes.2021.05.043.
[15] Z. Turakulov, A. Kamolov, A. Norkobilov, M. Variny, G. Díaz-Sainz, L. Gómez-Coma, M. Fallanza, Assessing various CO_2 utilization technologies: a brief comparative review, J. Chem. Technol. Biotechnol. 99 (2024) 1291–1307, https://doi.org/10.1002/jctb.7606.
[16] M.M. Ramirez-Corredores, G. Gadikota, E.E. Huang, A.M. Gaffney, Radiation-induced chemistry of carbon dioxide: a pathway to close the carbon loop for a circular economy, Front. Energy Res. 8 (2020) 1–17, https://doi.org/10.3389/fenrg.2020.00108.
[17] Q. Zhang, J. Peng, S. Jiang, H. Xiong, X. Fu, S. Shang, J. Xu, G. He, P.C. Chen, Plasma-activated 2D $CuMnO_2$ nanosheet catalysts with rich oxygen vacancies for efficient CO_2 electroreduction, Appl. Catal. Environ. 371 (2025), https://doi.org/10.1016/j.apcatb.2025.125255.
[18] L. Mastropasqua, L. Pierangelo, M. Spinelli, M.C. Romano, S. Campanari, S. Consonni, Molten carbonate fuel cells retrofits for CO_2 capture and enhanced energy production in the steel industry, Int. J. Greenh. Gas Control. 88 (2019) 195–208, https://doi.org/10.1016/j.ijggc.2019.05.033.
[19] S. Campanari, P. Chiesa, G. Manzolini, A. Giannotti, F. Federici, P. Bedont, F. Parodi, Application of MCFCs for active CO_2 capture within natural gas combined cycles, Energy Procedia 4 (2011) 1235–1242, https://doi.org/10.1016/j.egypro.2011.01.179.
[20] M. Spinelli, M.C. Romano, S. Consonni, S. Campanari, M. Marchi, G. Cinti, Application of molten carbonate fuel cells in cement plants for CO_2 capture and clean power generation, Energy Procedia 63 (2014) 6517–6526, https://doi.org/10.1016/j.egypro.2014.11.687.
[21] D.R. Nhuchhen, Integrated gasification carbon capture plant using molten carbonate fuel cell: an application to a cement industry, Energy 282 (2023), https://doi.org/10.1016/j.energy.2023.128614.
[22] R. Carapellucci, D. Di Battista, R. Cipollone, The retrofitting of a coal-fired subcritical steam power plant for carbon dioxide capture: a comparison between MCFC-based active systems and conventional MEA, Energ. Conver. Manage. 194 (2019) 124–139, https://doi.org/10.1016/j.enconman.2019.04.077.
[23] B. Bosio, M. Archetti, E. Audasso, D. Bove, Process analysis of a molten carbonate fuel cell on-board application to reduce vessel CO_2 emissions, Chem. Eng. Process. - Process Intensif. 190 (2023) 109415, https://doi.org/10.1016/j.cep.2023.109415.
[24] M. Archetti, E. Audasso, B. Bosio, D. Bove, High temperature fuel cells to reduce CO_2 emission in the maritime sector, E3S Web Conf. 334 (2022), https://doi.org/10.1051/e3sconf/202233404013.
[25] A. Baccioli, A. Liponi, J. Milewski, A. Szczęśniak, U. Desideri, Hybridization of an internal combustion engine with a molten carbonate fuel cell for marine applications, Appl. Energy 298 (2021), https://doi.org/10.1016/j.apenergy.2021.117192.
[26] R. Risso, L. Cardona, M. Archetti, F. Lossani, B. Bosio, D. Bove, A review of on-board carbon capture and storage techniques: solutions to the 2030 IMO regulations, Energies 16 (2023), https://doi.org/10.3390/en16186748.
[27] T.A. Barckholtz, K.M. Taylor, S. Narayanan, S. Jolly, H. Ghezel-Ayagh, Molten carbonate fuel cells for simultaneous CO_2 capture, power generation, and H_2 generation, Appl. Energy 313 (2022), https://doi.org/10.1016/j.apenergy.2022.118553.
[28] A. Monforti Ferrario, F. Santoni, M. Della Pietra, M. Rossi, N. Piacente, G. Comodi, L. Simonetti, A system integration analysis of a molten carbonate electrolysis cell as an off-gas recovery system in a steam-reforming process of an oil refinery, Front. Energy Res. 9 (2021), https://doi.org/10.3389/fenrg.2021.655915.
[29] D. Monzer, R. Rivera-Tinoco, C. Bouallou, Investigation of the techno-economical feasibility of the power-to-methane process based on molten carbonate Electrolyzer, Front. Energy Res. 9 (2021) 1–15, https://doi.org/10.3389/fenrg.2021.650303.
[30] S.A. Grigoriev, V.N. Fateev, D.G. Bessarabov, P. Millet, Current status, research trends, and challenges in water electrolysis science and technology, Int. J. Hydrogen Energy 45 (2020) 26036–26058, https://doi.org/10.1016/j.ijhydene.2020.03.109.
[31] B. Na, K. Kim, S.N. Lim, J.Y. Woo, Y. Choa, S.A. Song, Enhancing performance of molten carbonate electrolysis cell via deposition of gold nanoparticles on anode, Int. J. Hydrogen Energy 49 (2024) 964–970, https://doi.org/10.1016/j.ijhydene.2023.10.194.
[32] A. Moreno, V. Cigolotti, M. Della Pietra, L. Leto, S.J. McPhail, International status of molten carbonate fuel cells technology 2015, Enea (2015). Available online, https://www.pubblicazioni.enea.it/download.html?task=download.send&id=120:international-status-of-molten-carbonate-fuel-cells-technology-2015&catid=3 (accessed on 31/07/2025).
[33] M. Farooque, H.C. Maru, Carbonate fuel cells: milliwatts to megawatts, J. Power Sources 160 (2006) 827–834, https://doi.org/10.1016/j.jpowsour.2006.04.127.
[34] M.Y. Ramandi, P. Berg, I. Dincer, Three-dimensional modeling of polarization characteristics in molten carbonate fuel cells using peroxide and superoxide mechanisms, J. Power Sources 218 (2012) 192–203, https://doi.org/10.1016/j.jpowsour.2012.06.062.
[35] A. Bodén, G. Lindbergh, A model for mass transport of molten alkali carbonate mixtures applied to the MCFC, J. Electrochem. Soc. 153 (2006) A2111, https://doi.org/10.1149/1.2338653.
[36] R. Carapellucci, R. Cipollone, D. Di Battista, Modeling and characterization of molten carbonate fuel cell for electricity generation and carbon dioxide capture, Energy Procedia 126 (2017) 477–484, https://doi.org/10.1016/j.egypro.2017.08.228.
[37] M.C. Law, V.C.C. Lee, C.L. Tay, Dynamic behaviors of a molten carbonate fuel cell under a sudden shut-down scenario: the effects on temperature gradients, Appl. Therm. Eng. 82 (2015) 98–109, https://doi.org/10.1016/j.applthermaleng.2014.11.083.
[38] L. Hu, I. Rexed, G. Lindbergh, C. Lagergren, Electrochemical performance of reversible molten carbonate fuel cells, Int. J. Hydrogen Energy 39 (2014) 12323–12329, https://doi.org/10.1016/j.ijhydene.2014.02.144.
[39] L. Hu, G. Lindbergh, C. Lagergren, Performance and durability of the molten carbonate electrolysis cell and the reversible molten carbonate fuel cell, J. Phys. Chem. C 120 (2016) 13427–13433, https://doi.org/10.1021/acs.jpcc.6b04417.
[40] E. Audasso, K.I. Kim, G. Accardo, H.S. Kim, S.P. Yoon, Investigation of molten carbonate electrolysis cells performance for H_2 production and CO_2 capture, J. Power Sources 523 (2022) 231039, https://doi.org/10.1016/j.jpowsour.2022.231039.
[41] D. Monzer, C. Bouallou, Production of synthetic gas by the co-electrolysis of H_2O and CO_2 in the molten carbonate electrolyzer, Int. J. Hydrogen Energy 52 (2024) 152–166, https://doi.org/10.1016/j.ijhydene.2023.03.402.
[42] D. Monzer, C. Bouallou, Dynamic exploration of a 1 MW molten carbonate electrolyzer: a modeling study approach, Int. J. Hydrogen Energy 56 (2024) 989–997, https://doi.org/10.1016/j.ijhydene.2023.12.194.
[43] L. Barelli, G. Bidini, G. Cinti, J. Milewski, High temperature electrolysis using molten carbonate Electrolyzer, Int. J. Hydrogen Energy 46 (2021) 14922–14931, https://doi.org/10.1016/j.ijhydene.2020.07.220.
[44] M.A. Reyes-Belmonte, A. Delgado, E. Díaz, J. González-Aguilar, M. Romero, Molten carbonates electrolyzer model for hydrogen production coupled to medium/low temperature solar power plant, ISES Sol. World Congr. 2017 - IEA SHC int. conf. Sol. Heat. Cool. Build. Ind. 2017, Proc (2017) 168–178, https://doi.org/10.18086/swc.2017.04.13.
[45] L. Hu, H. Ekstr, G. Lindbergh, C. Lagergren, A model for analysis of the porous nickel electrode polarization in the molten carbonate electrolysis cell, J. Of The Electrochem. Soc. 164 (2017) H5197–H5201, https://doi.org/10.1149/2.0311708jes.
[46] M.A. Murmura, S. Lo Conte, F. Santoni, M. Della Pietra, L. Turchetti, M.C. Annesini, Two-dimensional modeling and experimental investigation of an inverse molten carbonate fuel cell, J. Power Sources 573 (2023), https://doi.org/10.1016/j.jpowsour.2023.233103.
[47] F.R. Bianchi, B. Bosio, F. Conte, S. Massucco, G. Mosaico, G. Natrella, M. Saviozzi, Modelling and optimal management of renewable energy communities using reversible solid oxide cells, Appl. Energy 334 (2023) 120657, https://doi.org/10.1016/j.apenergy.2023.120657.
[48] B.M. Dash, B.O. Bouamama, K.M. Pekpe, M. Boukerdja, Prior knowledge-infused self-supervised learning and explainable AI for fault detection and isolation in PEM electrolyzers, Neurocomputing 594 (2024) 127871, https://doi.org/10.1016/j.neucom.2024.127871.
[49] L. Fu, A novel robust control for disturbed uncertain microbial fuel cell with noisy output, J. New Mater. Electrochem. Syst. 28 (2025) 76–84, https://doi.org/10.14447/jnmes.v28i1.a08.
[50] B. Flamm, C. Peter, F.N. Büchi, J. Lygeros, Electrolyzer modeling and real-time control for optimized production of hydrogen gas, Appl. Energy 281 (2021) 116031, https://doi.org/10.1016/j.apenergy.2020.116031.
[51] J.P. Perez-Trujillo, F. Elizalde-Blancas, M. Della Pietra, S.J. McPhail, A numerical and experimental comparison of a single reversible molten carbonate cell operating in fuel cell mode and electrolysis mode, Appl. Energy 226 (2018) 1037–1055, https://doi.org/10.1016/j.apenergy.2018.05.121.
[52] J.P. Pérez-Trujillo, F. Elizalde-Blancas, S.J. McPhail, M. Della Pietra, B. Bosio, Preliminary theoretical and experimental analysis of a molten carbonate fuel cell operating in reversible mode, Appl. Energy 263 (2020), https://doi.org/10.1016/j.apenergy.2020.114630.

[53] B. Bosio, N. Di Giulio, S.W. Nam, A. Moreno, An effective semi-empiric model for MCFC kinetics: theoretical development and experimental parameters identification, Int. J. Hydrogen Energy 39 (2014) 12273–12284, https://doi.org/10.1016/j.ijhydene.2014.04.119.
[54] E.J.F. Dickinson, A.J. Wain, The Butler-Volmer equation in electrochemical theory: origins, value, and practical application, J. Electroanal. Chem. 872 (2020) 114145, https://doi.org/10.1016/j.jelechem.2020.114145.
[55] R. Seeber, C. Zanardi, G. Inzelt, Links between electrochemical thermodynamics and kinetics, ChemTexts 1 (2015), https://doi.org/10.1007/s40828-015-0018-9.
[56] Seventh Edition Fuel Cell Handbook, 2004, https://doi.org/10.2172/834188.
[57] E. Audasso, B. Bosio, D. Bove, E. Arato, T. Barckholtz, G. Kiss, J. Rosen, H. Elsen, R. B. Gutierrez, L. Han, T. Geary, C. Willman, A. Hilmi, C.Y. Yuh, H. Ghezel-Ayagh, New, dual-anion mechanism for molten carbonate fuel cells working as carbon capture devices, J. Electrochem. Soc. 167 (2020) 084504, https://doi.org/10.1149/1945-7111/ab8979.
[58] S. Koomson, C.G. Lee, Comparison of gas phase transport effects between fuel cell and electrolysis cell modes of a 100 cm^2 class molten carbonate cell, J. Electroanal. Chem. 925 (2022) 116896, https://doi.org/10.1016/j.jelechem.2022.116896.
[59] J.A. Prins-Jansen, K. Hemmes, J.H.W. De Wit, An extensive treatment of the agglomerate model for porous electrodes in molten carbonate fuel cells - II. Quantitative analysis of time-dependent and steady-state model, Electrochim. Acta 42 (1997) 3601–3618, https://doi.org/10.1016/S0013-4686(97)00137-0.
[60] A.J. Appleby, S. Nicholson, The reduction of oxygen in molten lithium carbonate, J. Electroanal. Chem. 53 (1974) 105–119, https://doi.org/10.1016/0022-0728(74)80007-0.
[61] A.J. Appleby, S.B. Nicholson, Reduction of oxygen in alkali carbonate melts, J. Electroanal. Chem. 83 (1977) 309–328, https://doi.org/10.1016/S0022-0728(77)80176-9.
[62] N. Subramanian, B.S. Haran, P. Ganesan, R.E. White, B.N. Popov, Analysis of molten carbonate fuel cell performance using a three-phase homogeneous model, J. Electrochem. Soc. 150 (2003) A46, https://doi.org/10.1149/1.1522721.
[63] M.Y. Ramandi, P. Berg, I. Dincer, Numerical analysis of transient processes in molten carbonate fuel cells via impedance perturbations, J. Power Sources 231 (2013) 134–145, https://doi.org/10.1016/j.jpowsour.2012.12.104.
[64] L. Hu, G. Lindbergh, C. Lagergren, Electrode kinetics of the NiO porous electrode for oxygen production in the molten carbonate electrolysis cell (MCEC), Faraday Discuss. 182 (2015) 493–509, https://doi.org/10.1039/c5fd00011d.
[65] S.N. Liu, W. Su, W.Y. Lv, Z.F. Wei, C.L. Zeng, Electrochemical impedance spectroscopy studies of corrosion of two-phase Ni-Dy alloys in molten $(0.62Li,0.38K)_2CO_3$ at 650 °C, high temp, Mater. Process. 32 (2013) 443–449, https://doi.org/10.1515/htmp-2012-0160.
[66] C.Y. Yuh, J.R. Selman, Polarization of the molten carbonate fuel cell anode and cathode, J. Electrochem. Soc. 131 (1984) 2062–2069.
[67] R. Guidelli, R.G. Compton, J.M. Feliu, E. Gileadi, J. Lipkowski, W. Schmickler, S. Trasatti, Defining the transfer coefficient in electrochemistry: an assessment (IUPAC technical report), Pure Appl. Chem. 86 (2014) 245–258, https://doi.org/10.1515/pac-2014-5026.
[68] P. Ang, A.F. Sammells, Influence of electrolyte composition on electrode kinetics in the molten carbonate fuel cell, ECS Proc. 1981–10 (1981) 341–362, https://doi.org/10.1149/198110.0341pv.
[69] J. Jewulski, L. Suski, Model of the isotropic anode in the molten carbonate fuel cell, J. Appl. Electrochem. 14 (1984) 135–143, https://doi.org/10.1007/BF00618732.
[70] T. Nishina, M. Takahashi, I. Uchida, Gas Electrode Reactions in Molten Carbonate Media: IV. Electrode Kinetics and Mechanism of Hydrogen Oxidation in Eutectic, J. Electrochem. Soc. 137 (1990) 1112–1121, https://doi.org/10.1149/1.2086612.
[71] R. Weewer, K. Hemmes, J.H.W. de Wit, The mechanism of hydrogen oxidation at gold and nickel flag electrodes in molten Li/K carbonate, J. Electrochem. Soc. 142 (1995) 389–397, https://doi.org/10.1149/1.2044027.
[72] T.L. Wolf, G. Wilemski, Molten carbonate fuel cell performance model, J. Electrochem. Soc. 30 (1983) 48–55, https://doi.org/10.1149/1.2119681.
[73] G. DiGiuseppe, An electrochemical model of a solid oxide fuel cell using experimental data for validation of material properties, ASME 2010 8th int, Conf. Fuel Cell Sci. Eng. Technol. FUELCELL 2010 (2) (2010) 193–203, https://doi.org/10.1115/FuelCell2010-33248.
[74] D.F. Fairbanks, C.R. Wilke, Diffusion coefficients in multicomponent gas mixtures, Ind. Eng. Chem. 42 (1950) 471–475, https://doi.org/10.1021/ie50483a022.
[75] S. Koomson, C.G. Lee, Lifetime expectancy of molten carbonate fuel cells: part II. Cell life simulation using bench and coin-type cells, Int. J. Hydrogen Energy 46 (2021) 15052–15058, https://doi.org/10.1016/j.ijhydene.2020.07.217.
[76] C.G. Lee, J.Y. Hwang, M. Oh, D.H. Kim, H.C. Lim, Overpotential analysis with various anode gas compositions in a molten carbonate fuel cell, J. Power Sources 179 (2008) 467–473, https://doi.org/10.1016/j.jpowsour.2007.12.125.